Three-dimensional Venusian ionosphere model

Antoine Martinez, Jean-Yves Chaufray, Sébastien Lebonnois, Francisco Gonzàlez-Galindo, Franck Lefèvre, Gabriella Gilli

Icarus 415 (2024) 116035

Contents lists available at ScienceDirect

Icarus

journal homepage: www.elsevier.com/locate/icarus

Three-dimensional Venusian ionosphere model

Antoine Martinez [a,c,*], Jean-Yves Chaufray [b], Sébastien Lebonnois [a], Francisco Gonzàlez-Galindo [c], Franck Lefèvre [b], Gabriella Gilli [c]

[a] Laboratoire de Météorologie Dynamique, UMR 8539, IPSL, CNRS, Sorbonne Université, Paris, France
[b] LATMOS, CNRS, Sorbonne Université, Université Versailles St-Quentin, Paris, France
[c] Instituto de Astrofísica de Andalucía (IAA-CSIC), Glorieta de la Astronomía s/n, Granada, Spain

ARTICLE INFO

Keywords:
Venus
Ionosphere
Model

ABSTRACT

To study the Venusian ionosphere, a 3D ionospheric model is included in the Venus Planetary Climate Model (Venus PCM), which we present here with a number of recent extensions and improvements. Our ionospheric model of Venus consists of 15 charged species (electron and 14 ions), 13 photo-ionization for 8 species, an ion-neutral chemistry (61 reactions) and an ambipolar diffusion scheme for the ion vertical transport. The electron temperature is assumed independent of the solar activity. Simulation results are compared with observation from the Pioneer Venus (PV) and Venus Express (VEX) for high and low/intermediate solar activity respectively. The model shows that ambipolar diffusion dominates photochemical equilibrium above 180 km and above 130 km altitude on the dayside and the nightside respectively. On the dayside, the electron density predicted by Venus PCM and its variation with solar zenith angle (SZA) are in good agreement with PV observations at high solar activity, even if the secondary electron peak is underestimated by the model, due to the absence of (photo-) electron impact ionization process, in Venus PCM. At higher solar activity, the predicted horizontal and vertical variations in electron and ion densities are both significantly underestimated on the nightside, probably due to the currently predicted weak day-to-night transport and the absence of photo-electron impact ionization process which is the main source of ion production on the nightside. On the dayside at low solar activity, the electron density predicted by Venus PCM are over-estimated by a factor 1.25 at the altitude of the main ionospheric peak and by a factor 2–3 at 250 km, compared to VEX observations. We suggest that this difference between high and low solar activity is linked to the overestimation of the neutral density at low solar activity and the independence of electron temperature with solar activity used in Venus PCM, which should have a significant effect on ion chemistry and the scale height of ion species.

1. Introduction

The Pioneer Venus space mission provided the largest, most comprehensive and extensive in-situ study of the Venusian thermosphere and ionosphere between 1978 and 1992. Most of the in-situ observations of the neutral and ions species took place between 1978 and 1982 in the period of high solar activity, above 150 km altitude mainly and so there are no in situ data on the dayside about either the ions or the neutrals at low solar activity from PV measurements. The PV Orbiter Radio Occultation (ORO) experiment, however, provided electron density profiles throughout the 14 years of the mission, which covered the whole range of solar activity (e.g., Kliore and Mullen, 1989; Kliore, 1992; Fox and Kliore, 1997) and, more recently, the Venus Express Radio Science Experiment which covered the low and intermediate solar activity period (Häusler et al., 2006; Pätzold et al., 2007). These data have enabled us to gain a better knowledge of the composition of the Venusian ionosphere and thermosphere, as well as its vertical and horizontal variation in a context of high solar activity.

The composition of the upper neutral atmosphere of Venus is mainly composed of O (atomic oxygen) above ~155 km at noon (~140 km on the nightside), while CO_2 (carbon dioxide) dominates below. By interacting with the solar extreme ultraviolet radiation, these neutral species are ionized and formed the ions:

$$CO_2 + h\upsilon \rightarrow \begin{cases} CO_2^+ + e \\ CO + O^+ + e \\ CO^+ + O + e \end{cases}$$

* Corresponding author at: Laboratoire de Météorologie Dynamique, UMR 8539, IPSL, CNRS, Sorbonne Université, Paris, France.
E-mail address: antoine.martinez@lmd.ipsl.fr (A. Martinez).

https://doi.org/10.1016/j.icarus.2024.116035
Received 20 September 2023; Received in revised form 29 February 2024; Accepted 5 March 2024
Available online 7 March 2024

$$O + h\upsilon \rightarrow O^+ + e$$

The density peak of the ionosphere is located near 138–142 km at noon on Venus, corresponding to the peak of CO_2 photoionization, and essentially composed of O_2^+ although the O_2 (molecular oxygen) abundance on Venus is very low. This particularity is explained by the fast ion reaction scheme with O, O^+, CO^+, CO_2 and CO_2^+ summarized below:

$$CO_2{}^+ + O \rightarrow O^+ + CO_2$$

$$O^+ + CO_2 \rightarrow O_2{}^+ + CO$$

$$CO^+ + CO_2 \rightarrow CO_2{}^+ + CO$$

$$CO_2{}^+ + O \rightarrow O_2{}^+ + CO$$

This fast ion reaction scheme induces shorter chemical lifetimes of O^+ and CO_2^+ than that for O_2^+ when CO_2 dominates (Fehsenfeld et al., 1970). The amount of CO_2 decreases with altitude until it becomes negligible in comparison to atomic oxygen, making this reaction chain inefficient and giving way to O^+ which becomes dominant above ~190 km. The O_2^+ ions produced are mainly lost via dissociative recombination with electrons: $O_2^+ + e \rightarrow O + O$. The rate coefficient α_{dr} for this dissociative recombination reaction depends on the electronic temperature T_e: $2.0 * 10^{-7} * (300/T_e)^{0.7}$ $cm^3.s^{-1}$ for $T_e < 1200$ K and $7.4 * 10^{-8} * (1200/T_e)^{0.56}$ $cm^3.s^{-1}$ for $T_e \geq 1200$ K (Alge et al., 1983; Johnsen, 1987). Despite the importance of this parameter, measurements of electron temperature are limited to those from Electron Temperature Probe (ETP) instrument of Pioneer Venus Orbiter between 1978 et 1982, which also limits the temporal variability of this parameter, even if its diurnal evolution around the equator at high solar activity is observed. Also, we have no hint of the long term temporal variability of this parameter. In addition, the ETP measurements of T_e are limited to altitudes above 150 km (Theis, 1993) which excludes the peak of the ionosphere and causes an important uncertainty.

In spite of the many missions planned to study Venus's atmosphere (ENVISION, Davinci, Veritas, Venus Orbiter Mission (VOM), etc.), only VOM is slightly concerned with the thermosphere and ionosphere, and no more mission of this type is planned to date. So, reproducing these observations within a General Circulation Model (or Global Climate Model; GCM) and comparing them gives a better understanding of the physical processes at work and their extrapolation/prediction in the absence of sufficient observational data. We therefore included an ionospheric model in the Venus Planetary Climate Model (Venus PCM, formerly IPSL Venus GCM) which already reproduced the neutral Venusian atmosphere from the surface to the exosphere. (10^{-8} Pa, approximately 250 km at noon and 180–200 km on the nightside; Martinez et al., 2023; Gilli et al., 2017, 2021). The purpose of this work is to present the improvements made to the Venus PCM with the implementation of an ionospheric model, to estimate its validity and limits.

Section 2 presents the ionospheric model and the latest additions and improvements made in this version of the model. In the third section, we study the simulated Chapman layer, the vertical profiles and the ionospheric composition by comparison with data from Pioneer Venus and Venus Express missions. The effects of transport and the solar cycle are discussed. Conclusions are given in Section 4.

2. Venus PCM: Model description and recent improvements

The Venus PCM has been used to investigate all regions of the Venusian atmosphere as it covers the surface up to the lower thermosphere (140–160 km; Lebonnois et al., 2010, 2016; Gilli et al., 2017). The vertical grid was extended in Martinez et al. (2023), from 78 to 90 levels (180–250 km) using the vertical extension method detailed in Gilli et al. (2017) to cover the upper thermosphere and lower ionosphere. The horizontal resolution is 3.75° x 1.875° (96 longitudes × 96 latitudes) and the vertical grid has 90 pressure levels covering from ~$9.2{\cdot}10^6$ Pa to ~$8{\cdot}10^{-9}$ Pa. The vertical grid is not regular, with higher resolution close to the surface. The vertical model resolution is approximately ~2–3 km between 100 and 150 km, slightly smaller below 100 km and ~ 4–10 km above 150 km (0.01–0.4 scale height below 100 km and 0.4–0.8 scale height above). Conditions at the model upper boundary are similar to previous versions of the Venus PCM (sponge layer over the top four layers, with horizontal winds forced toward zonal average fields with timescale of the order of 1 Earth day in the top layer). Parameterizations for CO_2-O 15-μm cooling, non-LTE CO_2 near infrared heating, thermal conduction, molecular viscosity, extreme ultraviolet (EUV) heating and non-orographic gravity wave (GW) processes are presented and discussed in more detail in Gilli et al. (2017, 2021). This version uses an increased rate of the CO_2 photolysis into CO and $O(^1D)$ as detailed in Martinez et al. (2023). When the ionospheric model is activated, this tuning coefficient drops from 10 to 8.

With respect to the model described in Martinez et al. (2023) and Stolzenbach et al. (2023), the Venus PCM was updated with the inclusion of chemical reactions, the addition of nitrogen chemistry, an EUV dependence on photochemical scheme and the implementation of ionospheric chemistry. We describe below these improvements. Although the nitrogen chemistry is included in the current version of Venus PCM, it won't be studied in this article and will be described in more detail in forthcoming papers (Streel et al., 2023)." As an illustration, the composition of the main neutral species in the thermosphere of Venus at high solar activity (200 s.f.u) simulated by Venus PCM is shown in Fig. 1 in comparison with the observations made by PV-ONMS (Niemann et al., 1980).

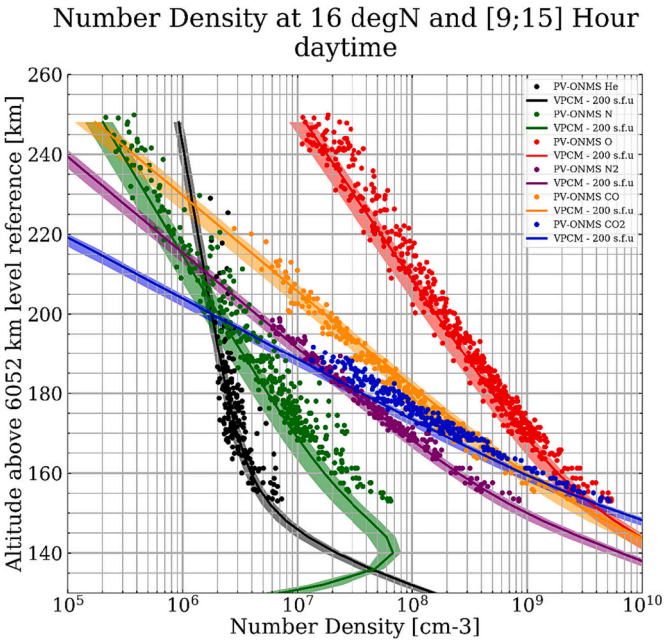

Fig. 1. Vertical profiles of the upper thermosphere number density composition (O: red; CO: yellow; CO_2: blue; N_2: purple, N: green; He: black) for E10.7 = 200 s.f.u (190 s.f.u < E10.7 < 210 s.f.u data restriction) conditions between 9 and 15 h local solar time. The points correspond to the PV-ONMS observations. The lines correspond to the densities predicted by the Venus PCM. The coloured areas correspond to the min/max variability of the corresponding number density. The modelled densities are not plotted above 250 km because the top of the model is close to this altitude. This figure and data are adapted from Martinez et al. (2023) and Niemann et al. (1980). (For interpretation of the references to colour in this figure legend, the reader is referred to the web version of this article.)

2.1. Upper atmosphere improvements

2.1.1. Neutral photochemical model

The current version of Venus PCM presented includes a full photochemical model of the Venus atmosphere (Stolzenbach et al., 2023, for the neutral chemical reaction list) which is based on the heritage of the Mars photochemical model (Lefèvre et al., 2004) and is briefly summarized in Gilli et al. (2017). Compared to the version described by Stolzenbach et al. (2023), the chemical network used here includes a description of the nitrogen chemistry with the addition of 4 new neutral species (N, N(^{2}D), NO and NO_2), 3 new photolysis reactions (involving N_2, NO_2 and NO) and 13 reactions. This addition will be detailed in a future paper in preparation (Streel et al., 2023). In total, our neutral chemical system takes into account 38 gas-phase and 2 liquid-phase species (Table 1) interacting through 119 neutral chemical reactions and 24 photodissociations.

The E10.7 solar flux values is used to characterize the EUV solar emission and the Solar Irradiance Platform v2.37 solar flux model is adopted (SIP; formerly SOLAR2000; https://spacewx.com/sip/) as reference. The E10.7 solar flux is adjusted for the Earth-Sun-Venus angle and distance but its magnitude, as displayed in figures, remains standardised to 1 AU. The choice of E10.7 instead of F10.7 in order to characterize the solar EUV flux is explained in Martinez et al. (2023). Unlike the lower atmosphere (below 100 km), thermospheric photochemistry is much more influenced by variations in extreme ultraviolet and ultraviolet (<200 nm) solar radiation with the solar activity cycle. In the Venus PCM version of Martinez et al. (2023) (and earlier), the photolysis rates are calculated for a fixed value of EUV solar radiation according to Atlas I solar spectrum reference (F10.7 = 192 s.f.u; Thuillier et al., 2004; E10.7 = 196 s.f.u). As a result, the production of CO and O(^{1}D) by photolysis of CO_2 was independent from EUV flux, which may lead to overestimate the density during the low and medium solar period above 100 km. In this study, the reference solar spectrum is an interpolation of two solar spectra: Atlas III solar spectrum reference (F10.7 = 77.5 s.f.u.; Thuillier et al., 2004; E10.7 = 97 s.f.u) and Atlas I solar spectrum reference. Above 192 s.f.u, we take only the Atlas I spectrum, and below 97 s.f.u, we limit the extrapolation of the spectrum until 70 s.f.u to avoid unrealistic extrapolation at loo-low values. This effect makes the photolysis dependent on the variation of the solar activity, parameterized by E10.7 proxy. To illustrate the change in production between the solar minimum and maximum achieved by this interpolation, Fig. 2 shows the vertical pressure profile of the ratio of atomic oxygen production by photochemistry between E10.7 = 200 s.f.u and 70 s.f.u.

The questions of whether or not more reference solar spectra or whether other reference solar spectra are needed for the interpolation are not studied here, but the nature of the interpolation and reference spectra may be updated in the future.

Table 1
List of chemical species in the Venus PCM. Top: neutral species. When several phase of the same species are considered: (g) stands for gas phases and (liq) for liquid phase. Bottom: charged species.

01 CO_2	09 O_3	17 HCl	25 SO_3	33 He
02 CO	10H	18 HOCl	26 S_2O_2	34 N_2
03 H_2	11 OH	19 ClCO	27 OCS	35 N
04 $H_2O_{(g)}$	12 HO_2	20 $ClCO_3$	28 HSO_3	36 N(^{2}D)
05 O(^{1}D)	13 H_2O_2	21 $COCl_2$	29 $H_2SO_{4(g)}$	37 NO
06 O(^{3}P) or O	14 Cl	22 S	30 S_2	38 NO_2
07 O_2	15 ClO	23 SO	31 $ClSO_2$	39 H_2O(liq)
08 O_2(a1Δg)	16 Cl_2	24 SO_2	32 OSCl	40 H_2SO_4(liq)
01 CO_2^+	09 H_2O^+			
02 CO^+	10 OH^+			
03 O^+	11C^+			
04 O_2^+	12 H_3O^+			
05H^+	13 HCO^+			
06 N_2^+	14 HCO_2^+			
07 N^+	15 e^-			
08 NO^+	10 OH^+			

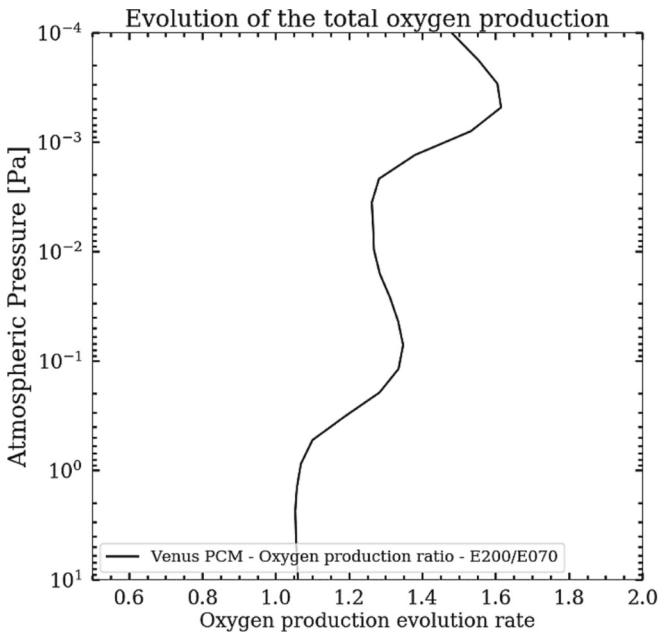

Fig. 2. Vertical pressure profile of the ratio of the atomic oxygen production at noon between the high (200 s.f.u) and the low solar activity (70 s.f.u).

2.1.2. Ionospheric chemistry model

One of the most important improvement to the Venus PCM compared with Martinez et al. (2023) is the addition of ion chemistry. This ionosphere model can only be activated and used when the model is extended at least as high as the exobase (200–250 km; 90 levels) since ionospheric processes only start to occur from the upper thermosphere (above 100–120 km with the main ionospheric peak at ~138–142 km). Based on the work presented in González-Galindo et al. (2013), the Venus PCM chemical model has thus been extended to include 13 photoionizations for 8 species (see Table 2) and 61 ionospheric reactions (see Table 3) between 15 charged species (see the bottom part of Table 1). The complete list of ion-neutral reactions only included in this version of the model can be seen in Table 3. When available, the reaction rates are taken from the JPL database, the UMIST compilation and reference within (see all references in Table 3). The atmosphere is forced to remain globally neutral, so that the electron concentration is equal to the sum of the concentrations of the different ions.

Contrary to the version of González-Galindo et al. (2013), the ionization caused by energetic photo-electrons is not included in this model.

Table 2
Table of photoionization included in Venus PCM. The ionization/dissociation branching ratio are extracted from Schunk and Nagy (2000) for CO_2, CO, O_2 and N_2. Because the atomic carbon is not included in the Venus PCM, the production of C by photoionization of CO_2 is not considered in this study.

N°	Photoionization
I01	$CO_2 + h\upsilon \rightarrow CO_2^+ + e$
I02	$CO_2 + h\upsilon \rightarrow O^+ + CO + e$
I03	$CO_2 + h\upsilon \rightarrow CO^+ + O + e$
I04	$CO_2 + h\upsilon \rightarrow C^+ + O_2 + e$
I05	$O_2 + h\upsilon \rightarrow O_2^+ + e$
I06	$O + h\upsilon \rightarrow O^+ + e$
I07	$NO + h\upsilon \rightarrow NO^+ + e$
I08	$CO + h\upsilon \rightarrow CO^+ + e$
I09	$CO + h\upsilon \rightarrow C^+ + O + e$
I10	$N_2 + h\upsilon \rightarrow N_2^+ + e$
I11	$N_2 + h\upsilon \rightarrow N^+ + N + e$
I12	$N + h\upsilon \rightarrow N^+ + e$
I13	$H + h\upsilon \rightarrow H^+ + e$

Table 3
List of ion chemical reactions in the Venus PCM. The rate coefficient for reaction is in $cm^3.molecule^{-1}.s^{-1}$. In the literature, chemical reactions with a # (E01, E11, E16, E17, E20, E23, E24, E35-E40, E48 and E50) use the ion temperature T_i but in the Venus PCM we use the electron temperature T_e instead, in the absence of reliable observed ion temperature (only at high solar activity but low quality spatial variation).

N°	Reaction	Reaction rate k	Reference
E01#	$CO_2^+ + O_2 \rightarrow O_2^+ + CO_2$	$5.5 * 10^{-11} * (300/T_e)^{0.5}$	Anicich (1993)
E02	$CO_2^+ + O \rightarrow O^+ + CO_2$	$9.60 * 10^{-11}$	UMIST database, from Fehsenfeld et al. (1970)
E03	$CO_2^+ + O \rightarrow O_2^+ + CO$	$1.64 * 10^{-10}$	UMIST database, from Fehsenfeld et al. (1970)
E04	$O_2^+ + e \rightarrow O + O$	$2.0 * 10^{-7} * (300/T_e)^{0.7}$ if $T_e < 1200$ $7.4 * 10^{-8} * (1200/T_e)^{0.56}$ if $T_e \geq 1200$	Alge et al. (1983) Johnsen (1987)
E05	$O^+ + CO_2 \rightarrow O_2^+ + CO$	$9.4 * 10^{-10}$	UMIST database, from Adams et al. (1980) and Smith et al. (1978)
E06	$CO_2^+ + e \rightarrow CO + O$	$3.8 * 10^{-7} * (300/T_e)^{0.5}$	UMIST database, from Mitchell (1990)
E07	$CO_2^+ + NO \rightarrow NO^+ + CO_2$	$1.2 * 10^{-10}$	Anicich (1993)
E08	$O_2^+ + NO \rightarrow NO^+ + O_2$	$4.6 * 10^{-10}$	Anicich (1993)
E09	$O_2^+ + N_2 \rightarrow NO^+ + NO$	$1.0 * 10^{-15}$	Ferguson (1973)
E10	$O_2^+ + N \rightarrow NO^+ + O$	$1.0 * 10^{-10}$	Scott et al. (1998)
E11#	$O^+ + N_2 \rightarrow NO^+ + N$	$1.2 * 10^{-12} * (300/T_e)^{0.45}$	Hierl et al. (1997)
E12	$NO^+ + e \rightarrow N + O$	$4.3 * 10^{-7} * (300/T_e)^{0.37}$	UMIST database, from Mitchell (1990)
E13	$CO^+ + CO_2 \rightarrow CO_2^+ + CO$	$1.0 * 10^{-9}$	UMIST database, from Adams et al. (1978)
E14	$CO^+ + O \rightarrow O^+ + CO$	$1.4 * 10^{-10}$	UMIST database, from Fehsenfeld and Ferguson (1972)
E15	$C^+ + CO_2 \rightarrow CO^+ + CO$	$1.1 * 10^{-9}$	UMIST database, from Fahey et al. (1981)
E16#	$N_2^+ + CO_2 \rightarrow CO_2^+ + N_2$	$9.0 * 10^{-10} * (300/T_e)^{0.23}$	Dotan et al. (2000)
E17#	$N_2^+ + O \rightarrow NO^+ + N$	$1.33 * 10^{-10} * (300/T_e)^{0.44}$	Scott et al. (1999), Anicich (1993)
E18	$N_2^+ + CO \rightarrow CO^+ + N_2$	$7.4 * 10^{-11}$	UMIST database, from Adams et al. (1980) and Smith et al. (1978)
E19	$N_2^+ + e \rightarrow N + N$	$1.7 * 10^{-7} * (300/T_e)^{0.3}$	UMIST database from Peterson et al. (1998)
E20#	$N_2^+ + O \rightarrow O^+ + N_2$	$7.0 * 10^{-12} * (300/T_i)^{0.23}$	Scott et al. (1999), Anicich (1993)
E21	$N^+ + CO_2 \rightarrow CO_2^+ + N$	$7.5 * 10^{-10}$	UMIST database, from Adams et al. (1980) and Smith et al. (1978)
E22	$CO^+ + H \rightarrow H^+ + CO$	$4.0 * 10^{-10}$	UMIST database, from Scott et al. (1997)
E23#	$O^+ + H \rightarrow H^+ + O$	$5.66 * 10^{-10} * (T_e/300)^{0.36} * exp.^{(8.6/Te)}$	UMIST database, from Stancil et al. (1999)
E24#	$H^+ + O \rightarrow O^+ + H$	$6.86 * 10^{-10} * (T_e/300)^{0.26} * exp.^{(-224.3/Te)}$	UMIST database, from Stancil et al. (1999)
E25	$CO_2^+ + H_2 \rightarrow HCO_2^+ + H$	$9.5 * 10^{-10}$	UMIST database, from Copp et al. (1982)
E26	$HCO_2^+ + e \rightarrow H + O + CO$	$8.1 * 10^{-7} * (300/T_e)^{0.64}$	UMIST database, from Geppert et al. (2004)
E27	$HCO_2^+ + e \rightarrow OH + CO$	$3.2 * 10^{-7} * (300/T_e)^{0.64}$	UMIST database, from Geppert et al. (2004)
E28	$HCO_2^+ + e \rightarrow H + CO_2$	$6.0 * 10^{-8} * (300/T_e)^{0.64}$	UMIST database, from Geppert et al. (2004)
E29	$HCO_2^+ + O \rightarrow HCO^+ + O_2$	$1.0 * 10^{-9}$	UMIST database (without citation)
E30	$HCO_2^+ + CO \rightarrow HCO^+ + CO_2$	$7.8 * 10^{-10}$	UMIST database, from Prasad and Huntress Jr. (1980)

Table 3 (*continued*)

N°	Reaction	Reaction rate k	Reference
E31	$H^+ + CO_2 \rightarrow HCO^+ + O$	$3.5 * 10^{-9}$	UMIST database, from Smith et al. (1992)
E32	$CO_2^+ + H \rightarrow HCO^+ + O$	$4.5 * 10^{-10}$	Borodi et al. (2009)
E33	$CO^+ + H_2 \rightarrow HCO^+ + H$	$7.5 * 10^{-10}$	UMIST database, from Scott et al. (1997)
E34	$HCO^+ + e \rightarrow CO + H$	$2.4 * 10^{-7} * (300/T_e)^{0.69}$	UMIST database, from Mitchell (1990)
E35#	$CO_2^+ + H_2O \rightarrow H_2O^+ + CO_2$	$2.04 * 10^{-9} * (300/T_e)^{0.5}$	UMIST database, from Karpas et al. (1978)
E36#	$CO^+ + H_2O \rightarrow H_2O^+ + CO$	$1.72 * 10^{-9} * (300/T_e)^{0.5}$	UMIST database, from Huntress Jr. et al. (1980)
E37#	$O^+ + H_2O \rightarrow H_2O^+ + O$	$3.2 * 10^{-9} * (300/T_e)^{0.5}$	UMIST database, from Adams et al. (1980) and Smith et al. (1978)
E38#	$N_2^+ + H_2O \rightarrow H_2O^+ + N_2$	$2.3 * 10^{-9} * (300/T_e)^{0.5}$	UMIST database, from Adams et al. (1980) and Smith et al. (1978)
E39#	$N^+ + H_2O \rightarrow H_2O^+ + N$	$2.8 * 10^{-9} * (300/T_e)^{0.5}$	UMIST database, from Adams et al. (1980) and Smith et al. (1978)
E40#	$H^+ + H_2O \rightarrow H_2O^+ + H$	$6.9 * 10^{-9} * (300/T_e)^{0.5}$	UMIST database, from Smith et al. (1992)
E41	$H_2O^+ + O_2 \rightarrow O_2^+ + H_2O$	$4.6 * 10^{-10}$	UMIST database, from Rakshit and Warneck (1980)
E42	$H_2O^+ + CO \rightarrow HCO^+ + OH$	$5.0 * 10^{-10}$	UMIST database, from Jones et al. (1981).
E43	$H_2O^+ + O \rightarrow O_2^+ + H_2$	$4.0 * 10^{-11}$	UMIST database, from Viggiano et al. (1980)
E44	$H_2O^+ + NO \rightarrow NO^+ + H_2O$	$2.7 * 10^{-10}$	UMIST database, from Rakshit and Warneck (1980)
E45	$H_2O^+ + e \rightarrow H + H + O$	$3.05 * 10^{-7} * (300/T_e)^{0.5}$	UMIST database, from Rosén et al. (2000).
E46	$H_2O^+ + e \rightarrow H + OH$	$8.6 * 10^{-8} * (300/T_e)^{0.5}$	UMIST database, from Rosén et al. (2000).
E47	$H_2O^+ + e \rightarrow O + H_2$	$3.9 * 10^{-8} * (300/T_e)^{0.5}$	UMIST database, from Rosén et al. (2000).
E48#	$H_2O^+ + H_2O \rightarrow H_3O^+ + OH$	$2.1 * 10^{-9} * (300/T_e)^{0.5}$	UMIST database, from Huntress Jr. and Pinizzotto Jr. (1973)
E49	$H_2O^+ + H_2 \rightarrow H_3O^+ + H$	$6.4 * 10^{-10}$	UMIST database, from Rakshit and Warneck (1980)
E50#	$HCO^+ + H_2O \rightarrow H_3O^+ + CO$	$2.5 * 10^{-9} * (300/T_e)^{0.5}$	Adams et al. (1978)
E51	$H_3O^+ + e \rightarrow OH + H + H$	$3.05 * 10^{-7} * (300/T_e)^{0.5}$	UMIST database, from Novotný et al. (2010).
E52	$H_3O^+ + e \rightarrow H_2O + H$	$7.09 * 10^{-8} * (300/T_e)^{0.5}$	UMIST database, from Novotný et al. (2010).
E53	$H_3O^+ + e \rightarrow OH + H_2$	$5.37 * 10^{-8} * (300/T_e)^{0.5}$	UMIST database, from Novotný et al. (2010).
E54	$H_3O^+ + e \rightarrow O + H_2 + H$	$5.6 * 10^{-9} * (300/T_e)^{0.5}$	UMIST database, from Novotný et al. (2010).
E55	$O^+ + H_2 \rightarrow OH^+ + H$	$1.7 * 10^{-9}$	Smith et al. (1978).
E56	$OH^+ + O \rightarrow O_2^+ + H$	$7.1 * 10^{-10}$	UMIST database, from Prasad and Huntress Jr. (1980)
E57	$OH^+ + CO_2 \rightarrow HCO_2^+ + O$	$1.44 * 10^{-9}$	UMIST database, from Jones et al. (1981).
E58	$OH^+ + CO \rightarrow HCO^+ + O$	$1.05 * 10^{-9}$	UMIST database, from Jones et al. (1981).
E59	$OH^+ + NO \rightarrow NO^+ + OH$	$3.59 * 10^{-9}$	UMIST database, from Jones et al. (1981).
E60	$OH^+ + H_2 \rightarrow H_2O^+ + H$	$1.01 * 10^{-9}$	UMIST database, from Jones et al. (1981).
E61	$OH^+ + O_2 \rightarrow O_2^+ + OH$	$5.9 * 10^{-10}$	UMIST database, from Jones et al. (1981).

This secondary ionization has been shown on Mars (Fox et al., 1996) and on Venus (Fox, 2006) to be important for the simulation of the secondary electronic peak around 120–130 km, but has a minor impact at higher altitude.

The electronic temperature T_e is an important parameter that affects most ionospheric reaction rates, mainly the ones of dissociative recombination reactions. Yet, as mentioned previously in Introduction,

the ETP measurements of T_e are limited to altitudes above 150 km (Theis, 1993) and only for at high solar activity period, so for lower altitudes an uncertain interpolation needs to be used. Here, we are using the vertical profile of electronic temperature from the model of Theis et al. (1984) (see Fig. 3) who developed an empirical formula for electron temperature above 150 km altitude, based on Pioneer Venus Orbiter ETP data at high solar activity. We assume that electrons and neutrals are in thermal equilibrium below 130 km. We therefore interpolate the temperature of electrons between 150 and 130 km with an exponential adjustment to take into account the efficiency of heating.

The ion temperature of the chemical reactions in Table 3 has been replaced in the model by the electronic temperature. In practice, the ion temperature is lower than the electron temperature, leading to an underestimation of the reaction rates, which however does not exceed a factor of 2 in the worst case. One way of improving the model would be to obtain the dependence of ion and electron temperatures on solar activity, to better constrain it.

To compute the photoionization rates by EUV, we use the same strategy as the one described in Gonzalez-Galindo et al. (González-Galindo, 2005; González-Galindo et al., 2009; González-Galindo et al., 2013). The EUV heating rates and photoionization rates are computed from pre-calculated photo-absorption coefficients. These coefficients, integrated in 36 spectral subintervals of varying spectral width in the 1–800 nm spectre range, were tabulated as a function of the column density. From this tabulation, all the photo-absorption coefficients for each species are calculated by interpolation to the actual column amount and by a sum over the 36 spectral intervals. For information, the first 16 spectral intervals (those with sufficient energy to ionize the main components of the upper atmosphere of Venus) range from 0.1 to 90.8 nm. After this, we multiplied these photo-absorption rates for each species with the efficiency of ionization and with the branching ratio of Schunk and Nagy (2000) in order to determinate the photoionization rate. This scheme is deeply described in González-Galindo (2005). The variation of the UV solar flux with the 11-year solar cycle (parameterized by E10.7 proxy) is also included by following the previous calculation by González-Galindo et al. (2013) which reproduce the solar cycle between 1976 and 2012 (more than three solar cycles), rescaled to the averaged Planet-Sun distance. The interest of this method is to be much faster than the detailed spectral integration.

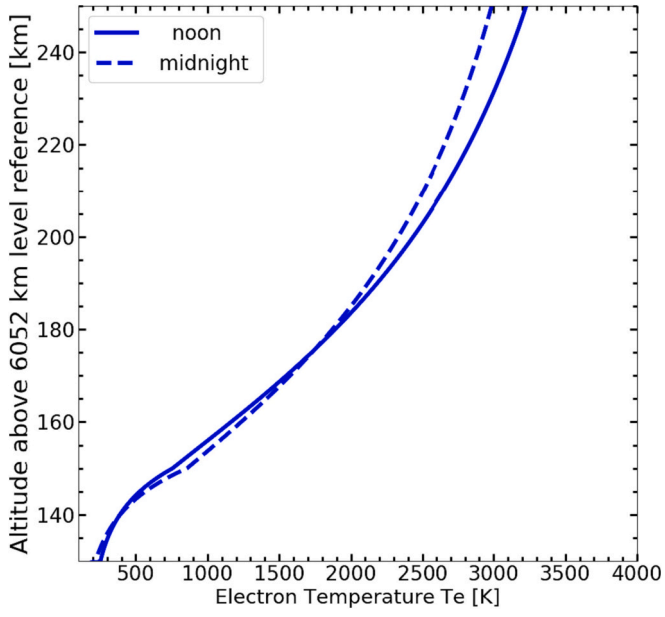

Fig. 3. Altitude profiles for the electron temperatures T_e adopted in the model. The solid curve is the case at noon and the dashed curve is the case at midnight. The electron temperatures are assumed to be independent of the solar cycle.

The ions, as the neutral species, are transported by the winds, so that their horizontal velocities are determined by the intensity of the general circulation. This ionospheric model is appropriate to the study of the photochemical region of the ionosphere (photochemistry equilibrium; PCE), below about 180 km. Above this altitude, plasma dynamics processes, as well as the interaction with magnetic fields, not included in the model, become important, so the results of the model are not reliable above that altitude. The effects of precipitating electrons are neither included in the model. The effects of the solar wind interaction with Venus is not included.

2.2. Implementation of the ambipolar diffusion

This section describes the efforts to improve the validity of the ionospheric model above 180 km by adding the vertical ion diffusion process based on the work of Chaufray et al. (2014). Above 180 km on the dayside, the characteristic time of ion transport processes (Bauer, 1973) becomes shorter than that of chemical processes (Banks and Kockarts, 1973, for the formulae). Indeed, with the small electron mass, gravity causes a slight charge separation, with the lighter electron tending to settle on the top of the heavier ions. This slight charge separation results in a polarization electrostatic field, which prevents a further charge separation. The electrons will be slowed down by the ions and the ions will be accelerated by the electrons. After this electrostatic field develops, the ions and electrons move together as a single gas under the influence of the temperature gradients, gravity and the density. This phenomenon is called ambipolar diffusion.

Thus, the model presented above is no longer able to reliably reproduce the vertical distribution of ionic species above a threshold altitude. We need to take account into this phenomenon by implementing the work of Chaufray et al. (2014) in Venus PCM. The horizontal component of ambipolar diffusion is not yet included in this study. This choice is explained by a limited effect of this horizontal transport on the density of ion species on the Martian nightside (Chaufray et al., 2014) and will be discussed for Venus in the next section.

We assume that the electro-neutrality (electron motion) is instantaneous. The mathematical development of the ambipolar diffusion equation is explained in Chaufray et al. (2014) and leads to eq. (1; Shinagawa and Cravens, 1988, 1989):

$$\left(\frac{\partial \rho_k}{\partial t}\right) = \frac{\partial}{\partial z}\left\{D_k\left(\frac{\partial \rho_k}{\partial z} + \rho_k\left[\frac{1}{T_k}\frac{\partial (T_k + T_e)}{\partial z} + \frac{T_e}{T_k}\frac{1}{\rho_e}\frac{\partial \rho_e}{\partial z} + \frac{1}{H_k}\right]\right)\right\} \quad (1)$$

where $D_k = k_B T_k / m_k \nu_k$ is the ambipolar diffusion coefficient of the ion k, k_B is the Boltzmann constant, T_e is the electron temperature, T_k is the ion temperature, ρ_e and ρ_k are respectively the electron and k^{th} ion density, $H_k = k_B T_k / m_k g$ is an atmospheric scale height. ν_k is the ion-neutral frequency for the k^{th} ion which is given by this calculation: $\nu_k = \sum_n \nu_{kn}$ with ν_{kn} from Banks and Kockarts (1973):

$$\nu_{kn} = 2.9 \times 10^{-9} \frac{m_n}{m_k + m_n} n_n \sqrt{\frac{\alpha_{pol,n}}{m_r}}$$

where $m_r = \frac{m_n m_k}{m_n + m_k}$ is the reduced mass of the n^{th} neutral species and the k^{th} ion species and $\alpha_{pol,n}$ is the polarizability of the n^{th} neutral species. The masses are in Da and the number densities are in cm^{-3}. In Chaufray et al. (2014), the choice was made to take only the $\alpha_{pol}(CO_2)$ and to consider that the entire atmosphere is made of CO_2, which is explained by the fact that CO_2 remains in the majority much higher up than on Venus (180–200 km compared with 140–155 km) for a similar top altitude model (200–250 km). Our choice to sum the ion-neutral frequencies for each neutral (here the main constituents of the upper thermosphere: CO_2, CO, O_2, O, N_2, N, He, H_2 and H) is linked to the gradient of composition with altitude in the Venus upper atmosphere. This variation as a function of altitude and SZA is faster than on Mars. For the same quantity of matter n_n, the frequency of ions with a medium

composed of H, O, N, H_2 or He will be lower than that with CO_2, which will tend to increase the ambipolar diffusion coefficient and therefore accelerate ambipolar diffusion compared with a thermosphere composed mainly of CO_2. The values of $\alpha_{pol,n}$ for each neutral species are extracted from *CRC Handbook of Chemistry and Physics (2004; p.3–150)*. For example, $\alpha_{pol}(CO_2) = 2.911 \times 10^{-24}\ cm^{-3}$, $\alpha_{pol}(O) = 0.802 \times 10^{-24}\ cm^{-3}$, $\alpha_{pol}(H_e) = 0.20550522 \times 10^{-24}\ cm^{-3}$ and $\alpha_{pol}(H) = 0.666793 \times 10^{-24}\ cm^{-3}$.

As in Chaufray et al. (2014), to solve the eq. (1), a finer vertical resolution is used above pressure level $P_0 = 7 * 10^{-4}$ Pa (~135 km at noon, ~130–125 km at midnight). The spatial resolution is not constant because we choose 168 grid points along the vertical and the altitude of the first and last pressure levels are not constants. Typical vertical resolution is 0.8 km in the dayside and 0.4 in the nightside. This increase in vertical resolution compared to Mars in Chaufray et al. (2014) is attributed to the stronger vertical variation of the composition on Venus. Too few points caused numerical artefacts around $7 * 10^{-4}$ Pa to $7 * 10^{-6}$ Pa due to the different distribution of points in the altitude grid on the pressure grid.

As eq. (1) is nonlinear due to the term involving the electron density, the forward-backward (predictor-corrector) scheme is used to solve it as described in Chaufray et al. (2014). A variable time step is used, dependent on the vertical velocity and the ambipolar diffusion coefficient computed at each time step. Typical time steps are between 0.008 and 4 s. The smaller time step is used to avoid numerical instabilities. The vertical velocity of each ion at the upper boundary is a free parameter chosen equal to 0 $km.s^{-1}$ (diffusive equilibrium). For the lower boundary ($P=P_0$), we assume that we are in the photochemical equilibrium ($\left(\frac{\partial \rho_k}{\partial t}\right)=0$).

Unlike chemical reactions, the ion temperature was taken as the maximum between the neutral temperature and 0.5 times the electron temperature. This choice was made because of the non-negligible influence of the ion temperature and its vertical and horizontal variations on the profile of the ions in the routine of the ambipolar diffusion. Although probably still overestimating the ion temperature, which will result in a larger ion scale height, the variations of the ion temperature are similar to that of the electron temperature vertically and horizontally.

All the simulations presented here have been done over one Venusian rotation (117 Earth days) and are initialized as in Martinez et al. (2023). Due to the speed of ion processes, the simulations started from a state without ion species in order to let the ionosphere form itself. For the reference simulation, we used: 5×10^{-12} $cm^3.s^{-1}$ for the CO_2-O deactivation rate within the experimental values: 1-6 $\times 10^{-12}$ $cm^3.s^{-1}$, 19.5% for the EUV heating efficiency and 70 and 200 s.f.u for the E10.7 solar flux index corresponding to solar 'low' and 'high' flux values. Due to the addition of ionospheric oxygen production, the tuning of the thermosphere on oxygen production presented in Martinez et al. (2023) has been modified by changing the factor from 10 to 8 in order to take this into account the additional production of atomic oxygen and to obtain a neutral atmosphere similar to the one presented in Martinez et al. (2023).

3. Results and discussion

The results discussed in this section were obtained using simulations of the Venus PCM described in Section 2. The aim of this section is to present a comprehensive comparison of these simulations, focusing on the ionosphere region (above 115–120 km) with datasets from several missions: Pioneer Venus and Venus Express. The altitude of the data was corrected to a common reference level ($z = 0$) corresponding to a radius of 6052 km above the centre of the planet. We took the distance to the centre of the planet of all observations ($R_i + z_i$), and subtracted it by the reference Venus radius. The instruments and measurements used in this validation are listed in Table 4. The geographical coverage (latitude, LT, SZA), altitude coverage and EUV conditions are also listed.

3.1. Main Chapman layer

As explained in Fox (2006), the Chapman layer theory (Chapman, 1931) has already been discussed and described in detail many times in articles and textbooks for planetary ionosphere (e.g., Bauer, 1973; Banks and Kockarts, 1973; Schunk and Nagy, 2000). So, a brief review will therefore be presented here, based on that of Fox (2006). A Chapman ion layer is produced in an isothermal thermosphere that is characterized by a neutral temperature T_n. The ions are produced by photoionization of a single molecular species, XY, by monochromatic radiation with a photon flux at the top of the atmosphere F^{∞} and a production rate $q_{i\chi}(z)$ where χ is the solar zenith angle. The more efficient way to destroy locally the molecular ions is the dissociative recombination with a rate coefficient α_{dr}. In a Chapman layer, the PCE prevails, so for a given χ, the production rate of the ions is equal to the loss rate due to the dissociative recombination:

$$q_i(z) = \alpha_{dr}\, n_i(z) * n_e(z) \backsimeq \alpha_{dr}\, [n_e(z)]^2$$

$$n_e(z) \backsimeq (q_i(z)/\alpha_{dr})^{0.5}$$

where the ion density $n_i(z)$ is almost equal to the electron density $n_e(z)$. In the case of Venus, the main dissociative recombination is the one of O_2^+ with $\alpha_{dr} = 2.00 * (300/T_e)^{0.7}$ for $T_e < 1200$ K (see Table 3) at the level of the main peak of the Chapman layer. The maximum rate of

Table 4
Observations of ions and electron number densities used in this paper. *: Here, for the E10.7 solar flux values, we adopted the Solar Irradiance Platform v2.37 solar flux model (SIP; formerly SOLAR2000; https://spacewx.com/sip/). The E10.7 solar flux index is adjusted for the Earth-Sun-Venus angle but its magnitude remains standardised to 1 AU. Here, the reference Venus radius is 6052 km. [(a)] Although the PVOIMS data go down to 160 km, our analysis is limited to observations above 200 km because the ion density below that altitude were overestimated due to a technical problem, detected by Pioneer Venus team (Miller et al., 1984; Brace and Kliore, 1991).

Instrument/Experiment	Method	Lat coverage	LT coverage	EUV coverage (E10.7)*	Altitude coverage	(Retrieved) variable	References
Pioneer Venus Orbiter	Radio Occultation & Model	−80 to 90°N	30–100° SZA	206 s.f.u	135–150 km	(Main Peak Electron number density and altitude)	Cravens et al. (1981)
Venus Express/VeRa	Radio Occultation	10–16°N	10–120° SZA	80–150 s.f.u	100–500 km	Electron number density	Häusler et al. (2006) ; Pätzold et al. (2007)
Pioneer Venus Orbiter Ions Mass Gas Spectrometer	Ion Mass Gas In-situ measurements	10–30°N	02–22H	180–260 s.f.u	200–350 km [(a)]	Ion composition, Number Density	Cloutier (1993)
Pioneer Venus Orbiter Electron Temperature Probe	In-situ measurements	10–30°N	0-24H	180–260 s.f.u	155–350 km	Electron number density, electron temperature	Theis (1993)

ionization at subsolar point is (e.g. Bauer, 1973):

$$q_{imax} = (F^{\infty}/e)^{*}(\sigma_i/\sigma_{tot})/H$$

σ_{tot} is the total photoabsorption cross section, σ_i is the photoionization cross section and H is the neutral pressure scale. Therefore, the maximum electron/ion density is proportional to $[F^{\infty}]^{0.5}$ and $T_e^{0.35}$. So, it is obvious from this dependency why a higher T_e and F^{∞} result in a larger n_e. To simplify, some studies prefer to use a formula with an EUV proxy like F10.7. For example, Kliore and Mullen (1989) find the following relationship for the evolution of the main peak density with the solar EUV index at the subsolar point: $N_0(F10.7) = N_0(150) * (F10.7/150)^{0.376}$, determined from the Radio Occultation observations of Pioneer Venus. At the altitude of the peak, the ion or electron density in a Chapman layer for a solar zenith angle χ is given by:

$$N_{i\chi} = n_{imax,0}{}^{*} [cos(\chi)]^{k}$$

where k is 0.5 for an ideal Chapman layer, for a plane parallel atmosphere. The plane parallel approximation is fairly accurate for solar zenith angles <60°, above 60°, the exponent k should be smaller than 0.5 and decrease monotonically as the terminator is approached due to the spherical geometry becoming more important. Another difference between real ionospheric layer and an ideal Chapman layer is that photoionization is supplemented by (photo-)electron-impact ionization. Because the more energetic photons penetrate to lower altitudes, the (photo-)electron-impact ionization rates usually peak lower in the ionosphere than do those due to photoionization.

The Venus PCM electron density at the main ionospheric peak and the altitude of this peak are compared to numerous Pioneer Venus (high solar activity) and Venus Express (low-intermediate solar activity) observations. We respectively find a factor k equal to 0.454 and 0.452 for the no-ambipolar and ambipolar version of the model and for SZA < 70°. This value is significantly lower than the exponent that Kliore and Mullen (1989) calculated (k = 0.511) but they included a larger range of solar zenith angle values. The model of Fox (2006) finds similar values with 0.43 for 60–70° SZA ranges. Our model therefore remains within the ranges of values of the observations and of the other models for the Chapman SZA dependency.

The variation of the simulated altitude of the ionospheric density peak with the solar zenith angle is in agreement with observations, with a value around 138–142 km at the subsolar point, and seem not to be significantly influenced by solar activity (see Fig. 4). Cravens et al. (1981) explained the nearly constant altitude peak over such a large solar zenith angle range as due to the "collapse" of the thermosphere as it merges into the nightside cryosphere, where the temperature and the neutral density are very low.

The variation of the main electron density peak of the Venusian ionosphere with the solar zenith angle for different data sets and different E10.7 is shown in Fig. 5. It can be seen that our model reproduces with good agreement the electron density peak at high solar activity (200 s.f.u) with a value of ~7.4–7.5 * 10^5 cm^{-3} at the subsolar point and ~ 5.4 * 10^5 cm^{-3} at 60°, similar to those in Cravens et al. (1981). However, our model at low solar activity (70 s.f.u) overestimates the electron density peak with a value of 5.7 * 10^5 cm^{-3} at the subsolar point and ~ 4.2 * 10^5 cm^{-3} at 60°, which is close to VEX observations at moderate solar activity (140 s.f.u; 5.6–6.0 * 10^5 cm^{-3} at subsolar point), giving a variation of the density peak of about 30% between the low and high solar activity. The model described in Fox and Sung (2001) finds a 60% variation of the Chapman density peak for a SZA of 60° between the minimum and maximum solar activity (80–200 s.f.u) with a constant electron temperature at the ionospheric density peak. Determining the dependence of electron density on E10.7 as performed in Kliore and Mullen (1989), we obtain an exponent of 0.26–0.27 for Venus PCM against 0.376 for Kliore and Mullen (1989) and 0.479–0.512 from the peak density values at high and low solar activity from the model of Fox and Sung (2001). Using the VEX electron density peak data for SZA < 70° to assure the flat atmosphere approximation, and correcting for SZA dependency (which amounts to dividing by $[\cos(\chi)]^k$ with here k = 0.5), a linear regression of these observations gives an EUV variation factor of 0.62–0.63, between 80 and 150 s.f.u., which is significantly higher than those for previous observations and modelling. These results about the influence of the solar activity will be discussed later.

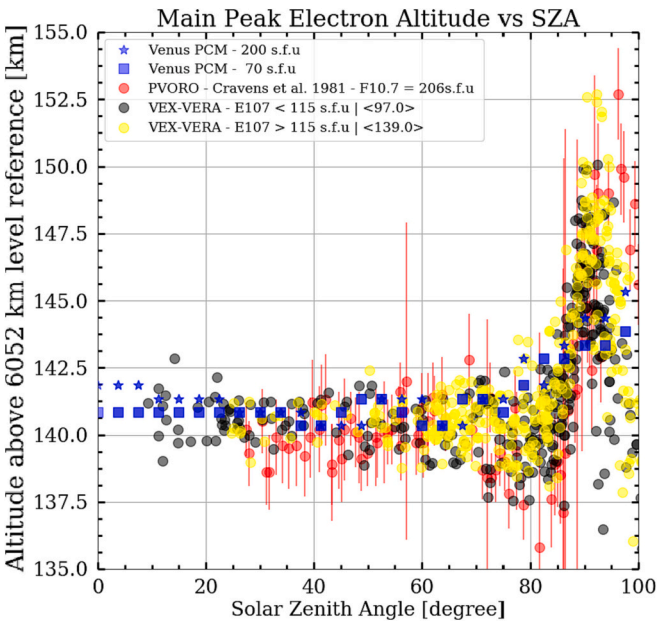

Fig. 4. Altitude of the main ionospheric peak versus solar zenith angle. The E10.7 solar flux index is adjusted for the Earth-Sun-Venus angle but its magnitude remains standardised to 1 AU. Red circles correspond to the data from Cravens et al. (1981) at high solar activity. Yellow and black circles correspond to the VEX observations for respectively low solar activity and intermediate solar activity conditions. Venus PCM results are in blue with 70 s.f.u for square points and 200 for star points. The <value> corresponds to the average E10.7 value for each selection of VEX-VERA data. (For interpretation of the references to colour in this figure legend, the reader is referred to the web version of this article.)

3.2. Simulated vertical profiles and ionosphere composition

The vertical profiles of the electron number density obtained with and without ion ambipolar diffusion for SZA < 20°, 50° < SZA < 60° and 100° < SZA < 110° and for different E10.7 compared to PV and VEX observations are displayed in Fig. 6. The difference in variability between the night-time observations of Pioneer Venus and Venus Express can be explained by the observation method used. In-situ observations of the upper atmosphere have smaller uncertainties than night-side radio occultation. On the dayside, the ambipolar diffusion has negligible effects below 160 km, affects the ionosphere above ~180 km and allows Venus PCM to reproduce the observations from PV-OETP very well at high solar activity. Ambipolar diffusion has more effects at lower altitude for higher solar zenith angle because photochemical forcing becomes less important, as we can see on the nightside with a strong effect above 130 km. We can also see that the secondary peak at 125 km on the dayside is underestimated by our model. This peak is initially created by wavelengths below 15 nm (soft X-ray), and this underestimation can be explained by two phenomena: Firstly, we have too low a spectral resolution below 5 nm (1 single bin), which can cause an underestimation of its effect as specified in González-Galindo et al. (2013), secondly, it is also due to the absence of (photo-)electron impact ionization, which is the main source of ionization below 130 km altitude.

Fig. 7 shows the ion number density in the lower ionosphere between

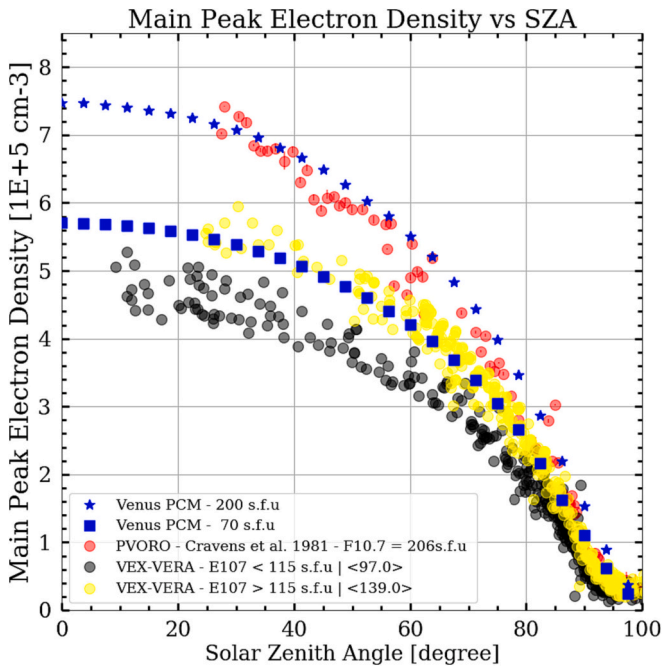

Fig. 5. Electron number densities at the ionospheric peak versus solar zenith angle. The E10.7 solar flux index is adjusted for the Earth-Sun-Venus angle but it magnitude remains standardised to 1 AU. Red circles correspond to the data from Cravens et al. (1981) at high solar activity. Yellow and black circles correspond to the VEX observations for respectively low solar activity and intermediate solar activity conditions. Venus PCM results are in blue with 70 s.f.u for square points and 200 for star points. The <value> corresponds to the average E10.7 value for each selection of VEX-VERA data. (For interpretation of the references to colour in this figure legend, the reader is referred to the web version of this article.)

08 h and 09 h local solar time predicted by no-ambipolar and ambipolar version of Venus PCM and compared to the PV-OIMS observations. As explained previously, although the PV-OIMS data go down to 160 km, we are limiting our analysis to observations above 200 km as a technical problem of Pioneer Venus caused a significant overestimation of the ions density below 200 km (Miller et al., 1984; Brace and Kliore, 1991). As observed, O_2^+ completely dominates the atmosphere below 160 km altitude, while O^+ takes over above 190 km altitude, which is similar to the model of Fox and Sung (2001). In the no-ambipolar version of the VPCM, the ionospheric peak around 220 km is mostly composed of O^+; this structure is explained by the photochemical equilibrium hypothesis. Indeed, ionic species density is mainly controlled by the fast reaction scheme seen in the introduction, which loses efficiency with altitude. So, if the peak at 140 km altitude corresponds to the equilibrium between ion production by CO_2 photoionization and O_2^+ destruction by dissociative recombination, the peak at 220 km corresponds to the equilibrium between O^+ photoionization and its chemical destruction in the absence of ambipolar diffusion. The O^+ density profile at photochemical equilibrium is very different from the one with ambipolar diffusion and presents a large upward density gradient, which leads to a strong downward flux as seen in Fig. 7. So, the O^+ peak density moves downward to 185 km where the ambipolar diffusion is activated.

With the ambipolar diffusion, the density profiles for CO_2^+ and O^+ are in better agreement with the PV-OIMS observations (see Fig. 7), and so is the electron density with the PV-OETP observations (see Fig. 6). However, above 200 km, predicted O^+ densities are ~60% of those measured by PV-OIMS, and there is overestimation of the O_2^+ density, probably due to the over-estimation of the ion temperature between 140 and 190 km which influences the scale height. Another indication of the effect of overestimating the electron temperature comes from the O^+ peak lying between 180 and 190 km, compared with 210 km in the paper by Fox and Sung (2001) which uses a lower ion temperature than ours and suggests that variations in electron and ion temperature have an influence on the density peak. Predicted CO_2^+ densities seem to be in the observation range of PV-OIMS. The underestimation of NO^+ and CO^+ density above 190 km altitude does not seem to be linked to an effect of ambipolar diffusion, but rather to a chemical effect, since these species already seemed to be underestimated without ambipolar diffusion. For these two species, the cause of the discrepancy is most likely due to chemical reaction rates and the neutral composition of the thermosphere below 180 km, in the PCE region.

3.2.1. *Ionospheric chemistry*

As with neutrals and molecular diffusion, the composition of the lower ionosphere will be greatly influenced by ionic (and neutral) composition below 180 km (in the PCE region), and will be controlled at higher altitudes by ambipolar diffusion. Studies of the ionospheric composition of Venus, meanwhile, are mostly limited to observations made by Pioneer Venus between 1978 and 1982 during the period of high solar activity, covering the whole dayside and much of the night, but only above 155 km, which limits the validation and improvement of ion chemistry. Because of the composition of its neutral thermosphere, which is chemically similar to that of Venus, the Martian observations and the difficulties of the Martian models to reproduce the MAVEN observations are of great interest for the development of Venusian ionospheric models. Mars has greater temporal and spatial coverage of the ionosphere thanks to recent observations by the MAVEN satellite since 2014 covering from 150 (intermediate solar activity) to 80 s.f.u (low solar activity), including the composition of the main ionospheric peak. As a result, many models have focused on reproducing ionospheric chemistry (Withers, 2023 and herein). They also present difficulties in reproducing observations in the PCE region, notably O_2^+, CO_2^+ and O^+, with the CO_2^+/O_2^+ ratio notably overestimated (Fox et al., 2021; Withers, 2023 and herein) at the ionospheric peak and O^+ underestimated in favour of O_2^+ and CO_2^+ at higher altitudes.

As the most important of all ion-neutral reactions is the charge exchange reaction between CO_2^+ and O, which can produce either O_2^+ and O^+ (see E02, E03 and E05 reactions in Table 3), these reaction rates have been investigated in order to explain these differences. Yet, the only two laboratory measurements of this pair of rate coefficients differ by an order of magnitude or more (Fehsenfeld et al., 1970; Tenewitz et al., 2018), as well as for the reaction rates calculation from composition (Fox et al., 2017, 2021). The conclusion of Fox et al. (2021) suggests that only the reactions rates from Fehsenfeld et al. (1970), although 50 years old, are much better at explaining the observed density profiles of O^+, O_2^+ and CO_2^+ on Mars, even if it remains significant difference with observations. The abundance of atomic oxygen is also an important parameter, as is the case for Venus (Martinez et al., 2023). So, in parallel with ambipolar diffusion, questions about ionospheric chemistry below 200 km need to be studied in greater depth on Venus (Fox and Sung, 2001; Fox, 2006), in line with Martian observations and models.

3.2.2. *Nightside and horizontal transport*

On the nightside, the effect of ambipolar diffusion is very significant, with a drastic change in the electron profile, as seen in Fig. 6. This is due to the fact that, in the presence of ambipolar diffusion, ions diffuse to lower altitudes where the density of neutrals is greater, and react very rapidly to form O_2^+ and NO^+, which are then destroyed by dissociative recombination. However, Ambipolar Venus PCM underestimates the density of ions and electrons by several orders of magnitude compared with PV-OIMS and PV-OETP observations, far more than the underestimation of the nightside martian ionosphere in the paper described by Chaufray et al. (2014). There are several possible explanations for this collapse:

- Firstly, on the Venusian nightside, a tenuous ionosphere is mainly maintained due to the plasma flow from dayside to nightside. (Fox

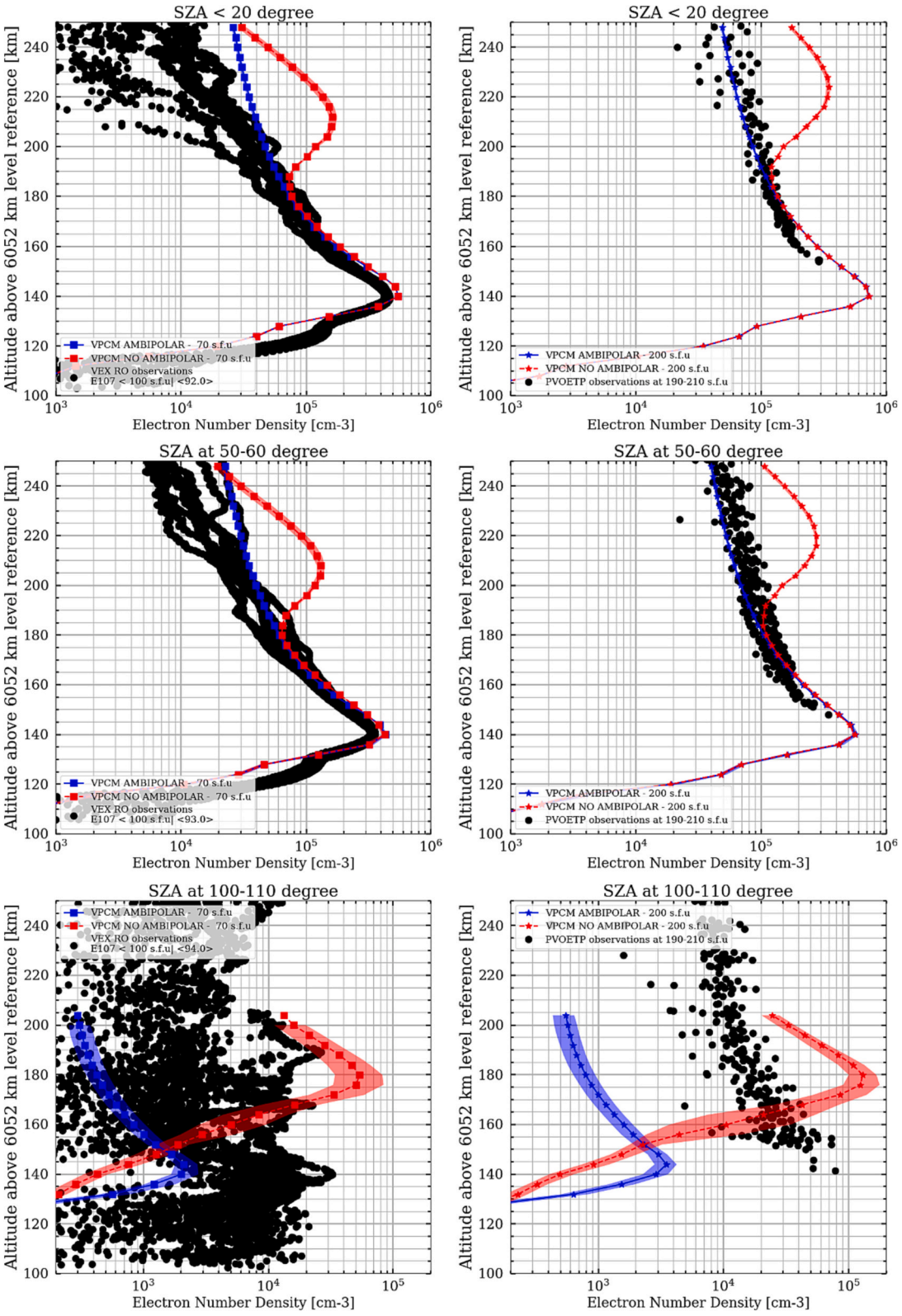

Fig. 6. Vertical profiles of the upper thermosphere electron number density for different solar zenith angles (top: < 20°, middle: 50–60° and bottom: 100–110°) and for different solar activity periods (left panel: low solar activity, right panel: high solar activity). Left panels: black circle points correspond to the Venus Express observations during Venus Express Radio Science Experiment (VeRa), during low solar activity. Right panels: black circle points correspond to the in-situ measurements from Pioneer Venus Orbiter ETP, during high solar activity. Red dashed curves correspond to the electron number density predicted by the "no ambipolar" version of Venus PCM. Blue curves correspond to the electron number density predicted by the "ambipolar" version of Venus PCM. The coloured areas correspond to the min/max variability of the electron number density of the corresponding version of Venus PCM. The modelled densities are not plotted above 250 km (200 km) because the top of the model is close to this altitude on the dayside (nightside). The <value> corresponds to the average E10.7 value for VEX-RO data. (For interpretation of the references to colour in this figure legend, the reader is referred to the web version of this article.)

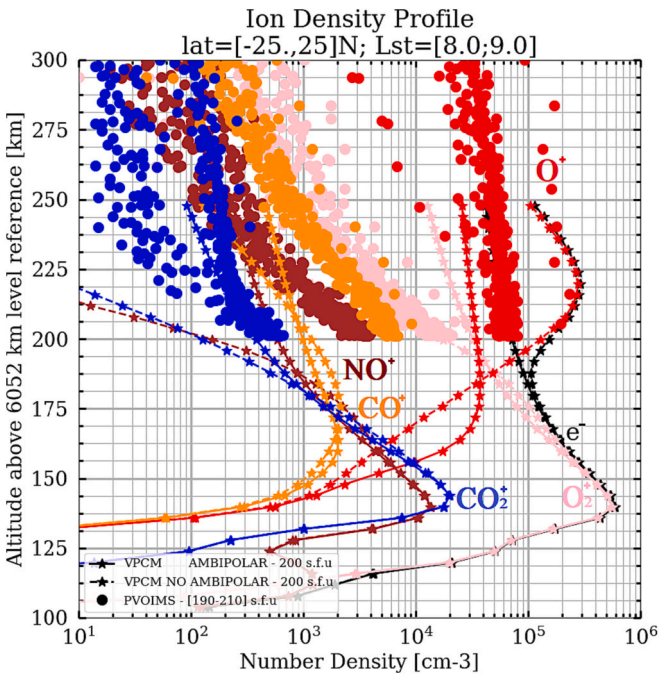

Fig. 7. Vertical profiles of the lower ionosphere (upper thermosphere region) number density composition (red: 16 amu (O^+), pink: 32 amu (O_2^+), orange: 28 amu (CO^+), brown: 30 amu (NO^+), blue: 44 amu (CO_2^+) and black: electron) between 08 h and 09 h local solar time. The circle points correspond to the PVOIMS observations. The full star lines correspond to the densities predicted by the "ambipolar" version of Venus PCM. The dashed star lines correspond to the densities predicted by the "no-ambipolar" version of Venus PCM. The modelled densities are not plotted above 250 km because the top of the model is close to this altitude. (For interpretation of the references to colour in this figure legend, the reader is referred to the web version of this article.)

and Kliore, 1997; Knudsen et al., 1981). Indeed, at high altitude but below the ionopause, the plasma flow from the subsolar region toward the nightside is primarily driven by the day-to-night pressure gradient and the momentum transfer from the solar wind above the ionopause. For instance, Knudsen et al. (1981) showed that the O^+ ions at the terminator have an antisunward velocity component of 2–3 km/s, and are accelerated nightward by the plasma pressure gradient force above 300 km up to the ionopause, which is an order of magnitude larger than that of neutrals. The average value of the antisunward component of the ion velocity in the terminator region at high solar activity increased with altitude from a few hundred m.s^{-1} at 150 km to ~4 km.s^{-1} at 800 km (below ionopause; Knudsen and Miller, 1992).

However, we have neglected the horizontal effect of ambipolar diffusion. So the ions are transported only by neutral winds in Venus PCM, which is slower and limit the ion horizontal transport. Indeed, in Chaufray et al. (2014), the authors explain that the horizontal diffusion has limited effect on the ion density on the nightside and that their Martian model underestimates the transterminator velocity by a factor 5 and so underestimate the ion transport from dayside to nightside. They suggested that the top of the model is too low for transport to be efficient, and that the difference in transterminator velocity with observations could be explained by the transport of ions by the solar wind via momentum transfer on Mars. Knudsen and Miller (1992), however, suggest that transport is dominated on Venus by the plasma pressure gradient, especially below the ionopause (300–1000 km according to the solar activity intensity).

- Secondly, the Venus PCM does not take into account electron impact processes, which are the main source of ionization on the nightside. Haider (1988) suggests that the electron impact ionization plays an important role in maintaining the ionosphere on the night side at low solar activity, when day-to-night ion transport is less efficient, even if the ion production rate by electron impact on the nightside is much lower than the dayside photoionization.

- Thirdly, the Venus PCM does not take into account the transport of ionic species by the solar wind (especially above the ionopause) which are much faster but also cause a loss term. This physical phenomenon is generally omitted due to its particularly high computational cost. These last three phenomena will therefore limit the contribution of new ion species on the nightside.

- Lastly, at low altitude, the chemical life of O_2^+, O^+ and CO_2^+ is much lower than at high altitude. The downward shift in the ion density peak will increase recombination losses. The characteristic time of recombination is much shorter than that of horizontal transport. Therefore, ambipolar diffusion will cause a drastic reduction in the density of ions and electrons, not compensated by the underestimated day-to-night horizontal transport. Chaufray et al. (2014) show less collapse on the nightside on Mars, yet as on Venus, horizontal transport time is greater than the chemical lifetime of ion species. This difference can be explained by the greater distance to be covered on the night side (The radius of Venus is 55% greater than that of Mars) and the length of nights on Venus, which is 120 times greater than on Mars, while horizontal transport times remain comparable. Adding horizontal transport by plasma pressure will increase the fluxes of ions and electron from day to night at the terminator. As a result, there would be a slight decrease in ion and electron density at high altitude on the dayside near the terminator, but an increase on the nightside.

So, our choice to neglect horizontal transport by the plasma pressure gradient was probably invalid on Venus, and would require further inclusion to estimate its effect on nightside ion density.

3.3. Solar activity variations

The orbit of Venus has a very low eccentricity (e = 0.0067) and a low obliquity (−2.63°). So, the seasonal effects are almost negligible and the main temporal variation in the ionosphere is due to the solar activity. However, no vertical profiles of the ion composition have been retrieved since Pioneer Venus in the 1980s and, unfortunately, no mission is currently planned for the next decades to measure the composition of the Venusian ionosphere and its ion/electron temperature. So, we have few constraints to reproduce the influence of the solar cycle on the properties of the ionosphere, its ion-neutral chemistry and to understand the role of the transport process. This will strongly limit the development and validation of GCMs. Due to the absence of evolution of the electronic and ionic temperature with solar activity within the Venus PCM, the evolution of the electron density is strictly due to the evolution of the photoionization rates linked to the solar spectrum and the neutral composition of the Venusian thermosphere.

Fig. 6 shows the variation of the vertical electron profile for low and high solar activity. On the dayside, Ambipolar Venus PCM reproduces electron density observations with good agreement, as well as the variation with altitude. At low solar activity, the model reproduces the evolution satisfactorily up to 190 km altitude, then underestimates the decay with altitude, probably due to a larger ionic scale height. This could be explained by our approximations of ion and electron temperatures. Indeed, we said earlier that we slightly overestimated ionic temperature, indexed on electronic temperature which is only suitable for high solar activity. So, the ion and electron temperatures are overestimated at low solar activity, leading to a larger ionic scale height. Moreover, a lower electron temperature induces more losses of O_2^+ by dissociative recombination, so reduces the electron number density

below 190 km. As it is already adapted to high solar activity, electronic temperature variations with E10.7 index will only modify low solar activity and improve the comparison. In addition, above 190 km, Martinez et al. (2023) have shown that the Venus PCM overestimates the mass density of Venus' atmosphere by a factor of 2 at 130 s.f.u around the equator on the dayside. It is therefore likely that part of the overestimation of electron density is linked to an overestimation of the neutral density of the upper thermosphere at low solar activity as seen in Martinez et al. (2023). Currently, the variation of the electron density at 250 km between 70 and 200 s.f.u is around a factor two for Venus PCM against at least 5 for observations.

At the level of the main Chapman peak, the Venus PCM reproduces the ionospheric peak during the high solar activity period (200 s.f.u) with good agreement with the data of Cravens et al. (1981) (see Fig. 5), but underestimates the variation between low and high solar activity with an overestimation by a factor ~ 1.2–1.25 at low solar activity period. As mentioned earlier, and like the model by Fox and Sung (2001) which could reproduce the variations of the ionospheric peak density with solar activity but underestimated its density in comparison to Cravens et al. (1981), our model uses an electron temperature independent of solar activity. The differences in the peak electron density dependency to solar cycle between the Venus PCM and the Fox and Sung (2001) model would therefore lie mainly in the change of the EUV solar spectrum, and therefore of electron production at the Chapman peak, which we overestimate at low solar activity. Comparison with observations is more difficult, however, because the density of the Chapman peak depends on the square root of electron production and electron temperature with an exponent of 0.35, and it is currently difficult to differentiate the contribution of electron production from that of electron temperature, due to the large uncertainties in determining the electron temperature at 140 km and its dependence in solar activity.

Although this subject is still under debate, some suggest that the electron temperature at the ionospheric peak could decrease by at least 25% from high to low solar activity, as in Kliore and Mullen (1989). If this variation was applied to our model, our low solar activity peak would decrease from 5.7 to 5.2 * 10^5 cm^{-3} at the subsolar point, which would still be 15% higher than VEX observations for a slightly larger observed E10.7 solar flux (90 s.f.u against 70 s.f.u used in the model).

The greater number of space missions on Mars means that it has a larger dataset representative of the evolution of the solar cycle, and the scientific community has taken an interest in the question of the variation of electronic temperature with solar activity, as in Vigren and Cui (2019) who used neutral data and O_2^+ chemistry to reconstruct the variation of electronic temperature with altitude at low solar activity, finding a value of electron temperature 2–3 times lower at 140 km than those of passed missions (~200 K vs ~500–600 K). In parallel, Hanley et al. (2021) used MAVEN's plasma instruments to reconstruct the electron temperature of Mars above 120 km altitude during the deep penetration phases of the spacecraft and observed that electron temperatures (300–700 K) remained much higher than the temperature of neutrals at 120 km altitude (120–170 K; about 1–3*10^{-4} Pa), while ions have a higher temperature than neutrals but to a lesser extent. This suggests that electrons and ions are no longer thermalized at these altitudes. Pilinski et al. (2023) built an empirical model of the variation of electron temperature with solar activity, and found a 7–12% variation in electronic temperature between mid and low solar activity period for a constant altitude above 160 km. The methods of Vigren and Cui (2019) and Kliore and Mullen (1989) could be applied to Venus data to enable a similar study in the future and better constrain the models. However, chemical reaction rates are important in these methods to determine chemical composition and electron temperature, which brings us back to our discussion about the uncertainty of chemistry reaction rates.

4. Conclusion

An ionospheric model has been implemented within the Venus PCM based on the work of González-Galindo et al. (2013) on the Martian ionosphere. It enables us to simulate the spatial and temporal variation of ion composition up to the top of the model, i.e. near the exobase. Ambipolar diffusion was also implemented as an option, based on the work of Chaufray et al. (2014) for Mars, and was adapted for the Venus ionosphere/thermosphere, notably by taking into account the change of composition with altitude and not taking into account the horizontal component of ambipolar diffusion in transport.

The altitude and spatial variation of the main ionospheric peak predicted by the model are in line with observations from Pioneer Venus during high solar activity (~200 s.f.u). On the dayside, the ambipolar diffusion widens the range of validity of the ionospheric model above 180 km (from 130 km on the night side) where this phenomenon becomes more important than photochemical equilibrium, and significantly modifies the distribution of ionic species like O^+ produced at high altitude. It also reproduces the profiles of the ionic composition of the lower ionosphere with altitude, although it underestimates the secondary ionosphere peak at 130 km because of the absence of photo-electron impact process. At low solar activity, Venus PCM overestimates peak electron density by 25% at 140 km and by a factor of 2–3 at 250 km compared with Venus Express/VeRa observations, probably due to electron temperature used in the reaction rate, which does not vary with solar activity, making the destruction and distribution of ionic species less efficient. The O^+ density peak is around 180–190 km against 210 km in Fox and Sung (2001), probably due to the overestimation of the ion temperature below 200 km.

On the nightside, pressure gradients transport the ions produced at high altitude to lower altitudes, helping to maintain a steady ionosphere. However, the electron density predicted by Venus PCM is underestimated by several orders of magnitude compared with PV-OETP observations. This is due to the efficiency of ion destruction by dissociative recombination, which cannot be compensated by nightside ion production and day-to-night transport. Added to this is the absence of ionization electron impact processes (the primary source of nightside ion production), the absence of horizontal plasma pressure gradient processes, and the absence of solar wind motion transfer.

Improving the prediction of the Venusian ionosphere by Venus PCM will be conditioned by future developments in ionospheric chemistry, ion and electron temperatures, and the implementation of new physical processes such as horizontal ambipolar diffusion and electron impact ionization and dissociation, which may also have a secondary impact on neutral composition. Finally, the transport of ions by motion transfer from the solar wind will be considered at the very end, due to the very high computational time required to resolve this phenomenon. A better determination of the electron temperature at the ionospheric density peak and its variation with solar activity is also envisaged, inspired by the work of Kliore and Mullen (1989) using the lastest VEX/VeRa data, and will be the subject of a future dependency study.

CRediT authorship contribution statement

Antoine Martinez: Writing – review & editing, Writing – original draft, Validation, Supervision, Methodology. **Jean-Yves Chaufray:** Methodology. **Sébastien Lebonnois:** Visualization, Funding acquisition. **Francisco Gonzàlez-Galindo:** Methodology. **Franck Lefèvre:** Methodology. **Gabriella Gilli:** Methodology.

Declaration of competing interest

The authors declare that they have no known competing financial interests or personal relationships that could have appeared to influence the work reported in this paper.

Data availability

Data will be made available on request.

Acknowledgement

The "PVO-V-OIMS-4-IONDENSITY-12S-V1.0" and "PVO-V-POS-5–VSOCOORDS-12SEC-V1.0" are obtained from the Planetary Data System (PDS) (https://pds.nasa.gov/). The Venus Express/Vera data set was provided by the RIU team (Cologne University), thank to them. This work was funded by ESA under the contract No. 4000130261/20/NL/CRS. The Venus PCM simulations were done thanks to the High-Performance Computing (HPC) resources of "Tres Grand Centre de Calcul" (TGCC) under the allocation n°A0140110391 made by Grand Equipement National de Calcul Intensif (GENCI). GG acknowledges financial support from Junta de Andalucia through the program EMERGIA 2021 (EMC21 00249). In parallel, the IAA team (A.M., F.G.-G., G.G.) were funded by Spanish Ministerio de Ciencia, Innovación y Universidades, the Agencia Estatal de Investigación and EC FEDER funds under projects RTI2018-100920-J-I00, PGC2018-101836-B-100, and PID2022-137579NB-I00 and A.M. acknowledges financial support from the Severo Ochoa grant CEX2021-001131-S funded by MCIN/AEI/ 10.13039/501100011033. A.M. and G.G. also acknowledge financial support from Junta de Andalucía through the program EMERGIA 2021 (EMC21 00249).

References

Adams, N.G., Smith, D., Grief, D., 1978. Reactions of H_nCO^+ ions with molecules at 300 K. Int. J. Mass Spectrom. 26 (4), 405–415. Elsevier BV. https://doi.org/10.1016/0020-7381(78)80059-x.

Adams, N.G., Smith, D., Paulson, J.F., 1980. An experimental survey of the reactions of NH_n^+ ions (n = 0 to 4) with several diatomic and polyatomic molecules at 300 K. J. Chem. Phys. 72 (1), 288–297. AIP publishing. https://doi.org/10.1063/1.438893.

Alge, E., Adams, N.G., Smith, D., 1983. Measurements of the dissociative recombination coefficients of O_2^+, NO^+ and NH_4^+ in the temperature range 200-600K. J. Phys. B Atomic Mol. Phys. 16 (8), 1433–1444. IOP publishing. https://doi.org/10.1088/0022-3700/16/8/017.

Anicich, V. G. (1993). Evaluated bimolecular ion-molecule gas phase kinetics of positive ions for use in modeling planetary atmospheres, cometary Comae, and interstellar clouds. J. Phys. Chem. Ref. Data (22, issue 6, pp. 1469–1569). AIP publishing. doi:https://doi.org/10.1063/1.555940.

Banks, W.H., Kockarts, G., 1973. Aeronomy. Academic, New York.

Bauer, S.J., 1973. Physics of Planetary Ionospheres. Springer, New York.

Borodi, G., Luca, A., & Gerlich, D. (2009). Reactions of CO_2^+ with H, H_2 and deuterated analogues. Int. J. Mass Spectrom. (280, issues 1–3, pp. 218–225). Elsevier BV. doi:https://doi.org/10.1016/j.ijms.2008.09.004.

Brace, L. H., & Kliore, A. J. (1991). The structure of the Venus ionosphere. Space Science Reviews (55, issues 1–4). Springer science and business media LLC. doi:https://doi.org/10.1007/bf00177136.

Chapman, S. (1931). The absorption and dissociative or ionizing effect of monochromatic radiation in an atmosphere on a rotating earth. Proc. Phys. Soc. (43, issue 1, pp. 26–45). IOP publishing. doi:https://doi.org/10.1088/0959-5309/43/1/305.

Chaufray, J.-Y., Gonzalez-Galindo, F., Forget, F., Lopez-Valverde, M., Leblanc, F., Modolo, R., Hess, S., Yagi, M., Blelly, P.-L., & Witasse, O. (2014). Three-dimensional Martian ionosphere model: II. Effect of transport processes due to pressure gradients. J. Geophys. Res. Planets (119, issue 7, pp. 1614–1636). Am. Geophys. Union doi:https://doi.org/10.1002/2013je004551.

Cloutier, P., 1993. PVO VENUS ION MASS SPECTROMTER LOW RES ION DENSITY V1.0 [Data Set]. NASA Planetary Data System. https://doi.org/10.17189/1519815.

Copp, N.W., Hamdan, M., Jones, J.D.C., Birkinshaw, K., Twiddy, N.D., 1982. A selected ion flow tube study of the reactions of the gaseous ion CO_2^+ at 298 K. Chem. Phys. Lett. 88 (5), 508–511. Elsevier BV. https://doi.org/10.1016/0009-2614(82)83164-3.

Cravens, T. E., Kliore, A. J., Kozyra, J. U., & Nagy, A. F. (1981). The ionospheric peak on the Venus dayside. J. Geophys. Res. (86, issue A13, p. 11323). American Geophysical Union (AGU). doi:https://doi.org/10.1029/ja086ia13p11323.

Lide, D.R. (Ed.), 2004. CRC Handbook of Chemistry and Physics, 85th ed. CRC Press, Boca Raton, FL.

Dotan, I., Midey, A. J., & Viggiano, A. A. (2000). Kinetics of the reactions of N_2^+ with CO_2 and SO_2 from 300–1400 K. J. Chem. Phys. (113, issue 5, pp. 1732–1737). AIP publishing. doi:https://doi.org/10.1063/1.481975.

Fahey, D.W., Fehsenfeld, F.C., Ferguson, E.E., 1981. Rate constant for the reaction $C^+ + CO_2$ at collision energies 0.04 to 2.5eV. Geophys. Res. Lett. 8 (10), 1115–1117. American Geophysical Union (AGU). https://doi.org/10.1029/gl008i010p01115.

Fehsenfeld, F.C., Ferguson, E.E., 1972. Thermal energy reaction rate constants for H+ and CO+ with O and NO. J. Chem. Phys. 56 (6), 3066–3070. AIP Publishing. https://doi.org/10.1063/1.1677642.

Fehsenfeld, F. C., Dunkin, D. B., & Ferguson, E. E. (1970). Rate constants for the reaction of CO_2^+ with O, O_2 and NO; N_2^+ with O and NO; and O_2^+ with NO. Planet. Space Sci. (18, issue 8, pp. 1267–1269). Elsevier BV. doi:https://doi.org/10.1016/0032-0633(70)90216-3.

Ferguson, E.E., 1973. Rate constants of thermal energy binary ion-molecule reactions of aeronomic interest. Atomic Data Nuclear Data Tables 12 (2), 159–178. Elsevier BV. https://doi.org/10.1016/0092-640x(73)90017-x.

Fox, J.L., 2006. Near-terminator Venus ionosphere: how Chapman-esque? J. Geophys. Res. 112, E04S02. https://doi.org/10.1029/2006JE002736.

Fox, J.L., Kliore, A.J., 1997. Ionosphere: Solar activity variations. In: Bougher, S., Hunten, D., Phillips, R. (Eds.), Venus II. Univ. of Ariz. Press, Tucson, pp. 161–188.

Fox, J.L., Sung, K.Y., 2001. Solar activity variations of the Venus thermosphere/ionosphere. J. Geophys. Res. 106 (A10), 21305–21335. https://doi.org/10.1029/2001ja000069.

Fox, J.L., Zhou, P., Bougher, S.W., 1996. The Martian thermosphere/ionosphere at high and low solar activities. Adv. Space Res. 17 (11), 203–218. Elsevier BV. https://doi.org/10.1016/0273-1177(95)00751-Y.

Fox, J.L., Johnson, A.S., Ard, S.G., Shuman, N.S., Viggiano, A.A., 2017. Photochemical determination of O densities in the Martian thermosphere: Effect of a revised rate coefficient. Geophys. Res. Lett. 44 (16), 8099–8106. American Geophysical Union (AGU). https://doi.org/10.1002/2017gl074562.

Fox, J.L., Benna, M., McFadden, J.P., Jakosky, B.M., 2021. Rate coefficients for the reactions of CO_2^+ with O: Lessons from MAVEN at Mars. In: Icarus, 358. Elsevier BV, p. 114186. https://doi.org/10.1016/j.icarus.2020.114186.

Geppert, W.D., Thomas, R., Ehlerding, A., Semaniak, J., Österdahl, F., Af Ugglas, M., Djurić, N., Paál, A., Larsson, M., 2004. Extraordinary branching ratios in astrophysically important dissociative recombination reactions. In: Faraday Discuss, 127. Royal Society of Chemistry (RSC), pp. 425–437. https://doi.org/10.1039/b314005a.

Gilli, G., Lebonnois, S., González-Galindo, F., López-Valverde, M.A., Stolzenbach, A., Lefèvre, F., Chaufray, J.Y., Lott, F., 2017. Thermal structure of the upper atmosphere of Venus simulated by a ground-to-thermosphere GCM. In: Icarus, 281. Elsevier BV, pp. 55–72. https://doi.org/10.1016/j.icarus.2016.09.016.

Gilli, G., Navarro, T., Lebonnois, S., Quirino, D., Silva, V., Stolzenbach, A., Lefèvre, F., Schubert, G., 2021. Venus upper atmosphere revealed by a GCM: II. Model validation with temperature and density measurements. In: Icarus, 366. Elsevier BV, p. 114432. https://doi.org/10.1016/j.icarus.2021.114432.

González-Galindo, F. (2005). Extension of a Martian general circulation model to thermospheric altitudes: UV heating and photochemical models. J. Geophys. Res. (110, issue E9). American Geophysical Union (AGU). doi:https://doi.org/10.1029/2004je002312.

González-Galindo, F., Forget, F., López-Valverde, M. A., Angelats Coll, M., & Millour, E. (2009). A ground-to-exosphere Martian general circulation model: 1. Seasonal, diurnal, and solar cycle variation of thermospheric temperatures. J. Geophys. Res. (114, issue E4). American Geophysical Union (AGU). doi:https://doi.org/10.1029/2008je003246.

González-Galindo, F., Chaufray, J.-Y., López-Valverde, M. A., Gilli, G., Forget, F., Leblanc, F., Modolo, R., Hess, S., & Yagi, M. (2013). Three-dimensional Martian ionosphere model: I. The photochemical ionosphere below 180 km. J. Geophys. Res. Planets (118, issue 10, pp. 2105–2123). American Geophysical Union (AGU). doi:https://doi.org/10.1002/jgre.20150.

Haider, S. A, 1988. Model calculations of nightside ionosphere of Venus - ionic composition. Ind. J. Radio Space 17 (5), 183–187.

Hanley, K. G., McFadden, J. P., Mitchell, D. L., Fowler, C. M., Stone, S. W., Yelle, R. V., Mayyasi, M., Ergun, R. E., Andersson, L., Benna, M., Elrod, M. K., & Jakosky, B. M. (2021). In situ measurements of thermal ion temperature in the Martian ionosphere. J. Geophys. Res. Space Physics (126, issue 12). American Geophysical Union (AGU). doi:https://doi.org/10.1029/2021ja029531.

Häusler, B., Pätzold, M., Tyler, G.L., Simpson, R.A., Bird, M.K., Dehant, V., Barriot, J.-P., Eidel, W., Mattei, R., Remus, S., Selle, J., Tellmann, S., Imamura, T., 2006. Radio science investigations by VeRa onboard the Venus express spacecraft. Planet. Space Sci. 54 (13–14), 1315–1335. Elsevier BV. https://doi.org/10.1016/j.pss.2006.04.032.

Hierl, P. M., Dotan, I., Seeley, J. V., Van Doren, J. M., Morris, R. A., & Viggiano, A. A. (1997). Rate constants for the reactions of O^+ with N_2 and O_2 as a function of temperature (300–1800 K). J. Chem. Phys. (106, issue 9, pp. 3540–3544). AIP publishing. doi:https://doi.org/10.1063/1.473450.

Huntress, W. T., Jr., & Pinizzotto, R. F., Jr. (1973). Product distributions and rate constants for ion-molecule reactions in water, hydrogen sulfide, ammonia, and methane. J. Chem. Phys. (59, issue 9, pp. 4742–4756). AIP publishing. doi:https://doi.org/10.1063/1.1680687.

Huntress Jr., W.T., Anicich, V.G., McEwan, M.J., Karpas, Z., 1980. Laboratory studies of some of the major ion-molecule reactions occurring in cometary comae. In: The Astrophysical Journal Supplement Series, 44. American Astronomical Society, p. 481. https://doi.org/10.1086/190701.

Johnsen, R., 1987. Microwave afterglow measurements of the dissociative recombination of molecular ions with electrons. In: International Journal of Mass Spectrometry and Ion Processes, 81. Elsevier BV, pp. 67–84. https://doi.org/10.1016/0168-1176(87)80006-x.

Jones, J. D. C., Birkinshaw, K., & Twiddy, N. D. (1981). Rate coefficients and product ion distributions for the reactions of OH^+ and H_2O^+ with N_2, O_2, NO. N_2O, Xe, CO, CO_2, H_2S and H_2 at 300 K. Chem. Phys. Lett. (77, issue 3, pp. 484–488). Elsevier BV. doi:https://doi.org/10.1016/0009-2614(81)85191-3.

Karpas, Z., Anicich, V.G., Huntress Jr., W.T., 1978. An ion cyclotron resonance study of reactions of some atomic and simple polyatomic ions with water. Chem. Phys. Lett. 59 (1), 84–86. Elsevier BV. https://doi.org/10.1016/0009-2614(78)85620-6.

Kliore, A.J., 1992. Radio occultation observations of the ionospheres of Mars and Venus. In: Luhmann, J.G., Tatrallyay, M., Pepin, R.O. (Eds.), Venus and Mars: atmospheres, ionospheres, and solar wind interactions. https://doi.org/10.1029/GM066p0265.

Kliore, A. J., & Mullen, L. F. (1989). The long-term behavior of the main peak of the dayside ionosphere of Venus during solar cycle 21 and its implications on the effect of the solar cycle upon the electron temperature in the main peak region. J. Geophys. Res. (94, issue A10, p. 13339). American Geophysical Union (AGU). doi:https://doi.org/10.1029/ja094ia10p13339.

Knudsen, W. C., & Miller, K. L. (1992). The Venus transterminator ion flux at solar maximum. J. Geophys. Res. (97, issue A11, p. 17165). American Geophysical Union (AGU). doi:https://doi.org/10.1029/92ja01460.

Knudsen, W.C., Spenner, K., Miller, K.L., 1981. Anti-solar acceleration of ionospheric plasma across the Venus terminator. Geophys. Res. Lett. 8 (3), 241–244. American Geophysical Union (AGU). https://doi.org/10.1029/gl008i003p00241.

Lebonnois, S., Hourdin, F., Eymet, V., Crespin, A., Fournier, R., & Forget, F. (2010). Superrotation of Venus' atmosphere analyzed with a full general circulation model. J. Geophys. Res. (115, issue E6). American Geophysical Union (AGU). doi:https://doi.org/10.1029/2009je003458.

Lebonnois, S., Sugimoto, N., Gilli, G., 2016. Wave analysis in the atmosphere of Venus below 100-km altitude, simulated by the LMD Venus GCM. In: Icarus, 278. Elsevier BV, pp. 38–51. https://doi.org/10.1016/j.icarus.2016.06.004.

Lefèvre, F., Lebonnois, S., Montmessin, F., & Forget, F.(2004). Three-dimensional modeling of ozone on Mars. J. Geophys. Res. (109, issue E7). American Geophysical Union (AGU). doi:https://doi.org/10.1029/2004je002268.

Martinez, A., Lebonnois, S., Millour, E., Pierron, T., Moisan, E., Gilli, G., Lefèvre, F., 2023. Exploring the variability of the venusian thermosphere with the IPSL Venus GCM. In: Icarus, 389. Elsevier BV, p. 115272. https://doi.org/10.1016/j.icarus.2022.115272.

Miller, K. L., Knudsen, W. C., & Spenner, K. (1984). The dayside Venus ionosphere. Icarus (57, 3, pp. 386–409). Elsevier BV. doi:https://doi.org/10.1016/0019-1035(84)90125-8.

Mitchell, A., 1990. The dissociative recombination of molecular ions. Phys. Rep. 186 (5), 215–248. Elsevier BV. https://doi.org/10.1016/0370-1573(90)90159-y.

Niemann, H.B., et al., 1980. Pioneer Venus orbiter neutral gas mass spectrometer experiment. IEEE Trans. Geosci. Remote Sens. 1, 60–65. https://doi.org/10.1109/TGRS.1980.350282.

Novotný, O., Buhr, H., Stützel, J., Mendes, M.B., Berg, M.H., Bing, D., Froese, M., Grieser, M., Heber, O., Jordon-Thaden, B., Krantz, C., Lange, M., Lestinsky, M., Novotny, S., Menk, S., Orlov, D.A., Petrignani, A., Rappaport, M.L., Shornikov, A., Schwalm, D., Zajfman, D., Wolf, A., 2010. Fragmentation channels in dissociative Electron recombination with hydronium and other Astrophysically important species. Chem. Eur. J. 114 (14), 4870–4874. American Chemical Society (ACS). https://doi.org/10.1021/jp9104097.

Pätzold, M., Häusler, B., Bird, M.K., Tellmann, S., Mattei, R., Asmar, S.W., Dehant, V., Eidel, W., Imamura, T., Simpson, R.A., Tyler, G.L., 2007. The structure of Venus' middle atmosphere and ionosphere. Nature 450 (7170), 657–660. Springer Science and Business Media LLC. https://doi.org/10.1038/nature06239.

Peterson, J. R., Le Padellec, A., Danared, H., Dunn, G. H., Larsson, M., Larson, A., Peverall, R., Strömholm, C., Rosén, S., Af Ugglas, M., & van der Zande, W. J. (1998). Dissociative recombination and excitation of N_2^+: cross sections and product branching ratios. J. Chem. Phys. (108, issue 5, pp. 1978–1988). AIP Publishing. doi:https://doi.org/10.1063/1.475577.

Pilinski, M.D., Andersson, L., Thiemann, E.M.B., 2023. An empirical model of electron temperatures in the Mars ionosphere based on Langmuir probe measurements in the descending phase of solar cycle 24. In: Icarus, 393. Elsevier BV, p. 114721. https://doi.org/10.1016/j.icarus.2021.114721.

Prasad, S.S., Huntress Jr., W.T., 1980. A model for gas phase chemistry in interstellar clouds. I - the basic model, library of chemical reactions, and chemistry among C, N, and O compounds. In: The Astrophysical Journal Supplement Series, 43. American Astronomical Society, p. 1. https://doi.org/10.1086/190665.

Rakshit, A.B., Warneck, P., 1980. Reactions of CO_2^+, $CO_2CO_2^+$ and H_2O^+ ions with various neutral molecules. J. Chem. Soc. Faraday Trans. 76, 1084, 2. Royal Society of Chemistry (RSC). https://doi.org/10.1039/f29807601084.

Rosén, S., Derkatch, A., Semaniak, J., Neau, A., Al-Khalili, A., Le Padellec, A., Vikor, L., Thomas, R., Danared, H., Af Ugglas, M., Larsson, M., 2000. Recombination of simple molecular ions studied in storage ring: Dissociative recombination of H_2O^+. In: Faraday Discussions, 115. Royal Society of Chemistry (RSC), pp. 295–302. https://doi.org/10.1039/a909314a.

Schunk, R.W., Nagy, A.F., 2000. Ionospheres. Cambridge University Press. https://doi.org/10.1017/cbo9780511551772.

Scott, G. B., Fairley, D. A., Freeman, C. G., McEwan, M. J., Spanel, P., & Smith, D. (1997). Gas phase reactions of some positive ions with atomic and molecular hydrogen at 300 K. J. Chem. Phys. (106, issue 10, pp. 3982–3987). AIP publishing. doi:https://doi.org/10.1063/1.473116.

Scott, G. B. I., Fairley, D. A., Freeman, C. G., McEwan, M. J., & Anicich, V. G. (1998). Gas-phase reactions of some positive ions with atomic and molecular nitrogen. J. Chem. Phys. (109, issue 20, pp. 9010–9014). AIP publishing. doi:https://doi.org/10.1063/1.477571.

Scott, G.B.I., Fairley, D.A., Milligan, D.B., Freeman, C.G., McEwan, M.J., 1999. Gas phase reactions of some positive ions with atomic and molecular oxygen and nitric oxide at 300 K. Chem. Eur. J. 103 (37), 7470–7473. American Chemical Society (ACS). https://doi.org/10.1021/jp9913719.

Shinagawa, H., & Cravens, T. E. (1988). A one-dimensional multispecies magnetohydrodynamic model of the dayside ionosphere of Venus. J. Geophys. Res. (93, issue A10, p. 11263). American Geophysical Union (AGU). doi:https://doi.org/10.1029/ja093ia10p11263.

Shinagawa, H., & Cravens, T. E. (1989). A one-dimensional multispecies magnetohydrodynamic model of the dayside ionosphere of Mars. J. Geophys. Res. Space Physics (94, issue A6, pp. 6506–6516). American Geophysical Union (AGU). doi:https://doi.org/10.1029/ja094ia06p06506.

Smith, D., Adams, N. G., & Miller, T. M. (1978). A laboratory study of the reactions of N^+, N_2^+, N_3^+, N_4^+, O^+, O_2^+, and NO^+ ions with several molecules at 300 K. J. Chem. Phys. (69, issue 1, p. 308). AIP publishing. doi:https://doi.org/10.1063/1.436354.

Smith, D., Spanel, P., Mayhew, C.A., 1992. A selected ion-flow tube study of the reactions of O^+, H^+ and HeH^+ with several molecular gases at 300 K. Int. J. Mass Spectrom. Ion Process. 117, 457–473. Elsevier BV. https://doi.org/10.1016/0168-1176(92)80108-d.

Stancil, P.C., Schultz, D.R., Kimura, M., Gu, J.-P., Hirsch, G., Buenker, R.J., 1999. Charge transfer in collisions of O+ with H and H+ with O. In: Astronomy and Astrophysics Supplement Series, 140. EDP Sciences, pp. 225–234. https://doi.org/10.1051/aas:1999419, 2.

Stolzenbach, A., Lefèvre, F., Lebonnois, S., Määttänen, A., 2023. Three-dimensional modeling of Venus photochemistry and clouds. In: Icarus, 395. Elsevier BV, p. 115447. https://doi.org/10.1016/j.icarus.2023.115447.

Streel, N., et al., 2023. 3D modelling of the Venus nitrogen chemistry. LPI Contrib. 2807. https://www.hou.usra.edu/meetings/venussurface2023/pdf/8021.pdf.

Tenewitz, J. E., Lê, T., Martinez, O., Jr., Ard, S. G., Shuman, N. S., Sanchez, J. C., Viggiano, A. A., & Melko, J. J. (2018). Kinetics of CO^+ and CO_2^+ with N and O atoms. J. Chem. Phys. (148, issue 8). AIP publishing. doi:https://doi.org/10.1063/1.5011195.

Theis, R., 1993. PVO VENUS ELECT TEMP PROBE DERVD ELECT DENS LOW RES VER 1.0 [Data Set]. NASA Planetary Data System. https://doi.org/10.17189/1519812.

Theis, R. F., Brace, L. H., Elphic, R. C., & Mayr, H. G. (1984). New empirical models of the electron temperature and density in the Venus ionosphere with application to transterminator flow. J. Geophys. Res. (89, issue A3, p. 1477). Am. Geophys. Union doi:https://doi.org/10.1029/ja089ia03p01477.

Thuillier, G., Floyd, L., Woods, T.N., Cebula, R., Hilsenrath, E., Hersé, M., Labs, D., 2004. Solar irradiance reference spectra for two solar active levels. Adv. Space Res. 34 (2), 256–261. Elsevier BV. https://doi.org/10.1016/j.asr.2002.12.004.

Viggiano, A.A., Albritton, D.L., Fehsenfeld, F.C., Adams, N.G., Smith, D., Howorka, F., 1980. Laboratory studies of some ion-atom reactions related to interstellar molecular synthesis. In: The Astrophysical Journal, 236. American Astronomical Society, p. 492. https://doi.org/10.1086/157766.

Vigren, E., Cui, J., 2019. Electron temperatures in the dayside ionosphere of Mars derived from O_2^+ chemistry. In: The Astrophysical Journal, 887. American Astronomical Society, p. 177. https://doi.org/10.3847/1538-4357/ab53db, 2.

Withers, P., 2023. Troubles in Mars ionosphere modeling. J. Geophys. Res. Space Phys. 128 (4) https://doi.org/10.1029/2022ja031227. Am. Geophys. Union.